CEP19–RABL2–IFT-B axis controls BBSome-mediated ciliary GPCR export

Zhuang Zhou, Yohei Katoh*, and Kazuhisa Nakayama*
Department of Physiological Chemistry, Graduate School of Pharmaceutical Sciences, Kyoto University, Sakyo-ku, Kyoto 606-8501, Japan

ABSTRACT **The intraflagellar transport (IFT) machinery mediates the import and export of ciliary proteins across the ciliary gate, as well as bidirectional protein trafficking within cilia. In addition to ciliary anterograde protein trafficking, the IFT-B complex participates in the export of membrane proteins together with the BBSome, which consists of eight subunits encoded by the causative genes of Bardet-Biedl syndrome (BBS). The IFT25–IFT27/BBS19 dimer in the IFT-B complex constitutes its interface with the BBSome. We show here that IFT25–IFT27 and the RABL2 GTPase bind the IFT74/BBS22–IFT81 dimer of the IFT-B complex in a mutually exclusive manner. Cells expressing GTP-locked RABL2 [RABL2(Q80L)], but not wild-type RABL2, phenocopied *IFT27*-knockout cells, that is, they demonstrated BBS-associated ciliary defects, including accumulation of LZTFL1/BBS17 and the BBSome within cilia and the suppression of export of the ciliary GPCRs GPR161 and Smoothened. RABL2(Q80L) enters cilia in a manner dependent on the basal body protein CEP19, but its entry into cilia is not necessary for causing BBS-associated ciliary defects. These observations suggest that GTP-bound RABL2 is likely to be required for recruitment of the IFT-B complex to the ciliary base, where it is replaced with IFT25–IFT27.**

Monitoring Editor
Gregory Pazour
University of Massachusetts

Received: May 6, 2022
Revised: Aug 24, 2022
Accepted: Sep 1, 2022

INTRODUCTION

Primary cilia are microtubule-based, membrane-sheathed protrusions from the surfaces of various eukaryotic cells and function as mechano- and chemosensors for extracellular stimuli and signaling molecules, such as the Hedgehog (Hh) family of morphogens (Anvarian *et al.*, 2019; Kopinke *et al.*, 2021). Owing to their crucial roles, dysfunction of cilia results in a range of genetic disorders with highly variable clinical manifestations, which are collectively referred to as the ciliopathies. These include Bardet-Biedl syndrome (BBS), Joubert syndrome, and Meckel syndrome (Braun and Hildebrandt, 2017; Reiter and Leroux, 2017). To act as sensory organelles, cilia have specific signaling components in the cilioplasm and on the ciliary membrane, including G protein-coupled receptors (GPCRs) and ion channels (Anvarian *et al.*, 2019; Nachury and Mick, 2019). Although the ciliary membrane is continuous with the plasma membrane, its distinct composition of ciliary proteins is maintained and regulated by the presence of the transition zone (TZ) at the ciliary base, which acts as a diffusion/permeability barrier (Garcia-Gonzalo and Reiter, 2017; Gonçalves and Pelletier, 2017).

Bidirectional protein trafficking along the axonemal microtubules is mediated by the intraflagellar transport (IFT) machinery, which contains the multisubunit IFT-A and IFT-B complexes. The IFT machinery also mediates import and export of proteins across the TZ (Rosenbaum and Witman, 2002; Taschner and Lorentzen, 2016; Nakayama and Katoh, 2018). The IFT-B complex, which is composed of 16 subunits, mediates anterograde protein trafficking powered by heterotrimeric kinesin-II (see Figure 7A). In addition, IFT-B regulates the export of ciliary membrane proteins across the TZ along with the BBSome (see Figure 7A), which is comprised of eight BBS proteins

This article was published online ahead of print in MBoC in Press (http://www.molbiolcell.org/cgi/doi/10.1091/mbc.E22-05-0161) on September 8, 2022.

Declaration of interests: The authors declare no competing interests in association with this study.

Author contributions: Z.Z. designed and performed the experiments; Y.K. and K.N. designed the experiments and prepared the manuscript.

*Address correspondence to: Kazuhisa Nakayama (kazunaka@pharm.kyoto-u.ac.jp); Yohei Katoh (ykatoh@pharm.kyoto-u.ac.jp).

Abbreviations used: BBS, Bardet-Biedl syndrome; cryo-ET, cryoelectron tomography/tomographic; DA, distal appendage; FBS, fetal bovine serum; GPCR, G protein-coupled receptor; GST, glutathione S-transferase; hTERT-RPE1, human telomerase reverse transcriptase-immortalized retinal pigment epithelial 1; IFT, intraflagellar transport; Hh, Hedgehog; KO, knockout; mChe, mCherry; Nb, nanobody; ROI, region of interest; SAG, Smoothened Agonist; SMO, Smoothened; tBFP, TagBFP; TZ, transition zone; VIP, visible immunoprecipitation.

(BBS1/BBS2/BBS4/BBS5/BBS7/BBS8/BBS9/BBS18) and the ARL6/BBS3 GTPase (Lechtreck *et al.*, 2013; Eguether *et al.*, 2014; Liew *et al.*, 2014; Liu and Lechtreck, 2018; Nozaki *et al.*, 2018; Ye *et al.*, 2018; Nozaki *et al.*, 2019; Zhou *et al.*, 2022). Recent studies suggested that the BBSome-mediated export of ciliary GPCRs requires their polyubiquitination (Desai *et al.*, 2020; Shinde *et al.*, 2020; Lv *et al.*, 2021). On the other hand, the IFT-A complex, which is comprised of six subunits, mediates retrograde protein trafficking powered by the dynein-2/IFT dynein complex (see Figure 7A). Furthermore, along with the TULP3 adaptor protein, IFT-A regulates the import of ciliary membrane proteins across the TZ (see Figure 7A) (Mukhopadhyay *et al.*, 2010; Park *et al.*, 2013; Badgandi *et al.*, 2017; Hirano *et al.*, 2017; Picariello *et al.*, 2019; Kobayashi *et al.*, 2021).

The 16 subunits of the IFT-B complex can be grouped into two subcomplexes: the core (IFT-B1) subcomplex composed of 10 subunits and the peripheral (IFT-B2) subcomplex composed of six subunits (Figure 1A). A tetrameric unit, containing two core subunits (IFT52 and IFT88) and two peripheral subunits (IFT38 and IFT57), constitutes the interface between the two subcomplexes (Boldt *et al.*, 2016; Katoh *et al.*, 2016; Taschner *et al.*, 2016) and acts as the binding site for heterotrimeric kinesin-II (Funabashi *et al.*, 2018; Nakayama and Katoh, 2020). Two core subunits, IFT74 and IFT81, form a tight heterodimer via their long coiled-coils and play a crucial role in the IFT-B complex. In particular, the IFT74–IFT81 dimer is essential for cilia biogenesis by directly binding to the α/β-tubulin dimer via their N-terminal regions (Figure 1B) (Bhogaraju *et al.*, 2013; Kubo *et al.*, 2016). In addition, the IFT74–IFT81 heterodimer acts as a hub in the IFT-B complex via interacting with IFT22, the IFT25–IFT27 dimer, and the IFT46–IFT52 dimer (Figure 1, A and B) (Taschner *et al.*, 2011; Taschner *et al.*, 2014; Katoh *et al.*, 2016; Wachter *et al.*, 2019; Zhou *et al.*, 2022). IFT25 and IFT27 form a tight heterodimer (Bhogaraju *et al.*, 2011) and participate in BBSome-mediated retrograde trafficking/export of ciliary membrane proteins (Keady *et al.*, 2012; Eguether *et al.*, 2014; Liew *et al.*, 2014; Dong *et al.*, 2017; Liu *et al.*, 2021; Sun *et al.*, 2021), although the precise mechanism is still controversial; in one proposed model, IFT-B-separated IFT25–IFT27 promotes ARL6 activation and the subsequent assembly of the BBSome at the ciliary tip to mediate retrograde trafficking (Liew *et al.*, 2014); and in another model, LZTFL1/BBS17 connects the BBSome to IFT25–IFT27 to export ciliary membrane proteins across the TZ (Figure 1A; also see Figure 7A), although there is no evidence for an interaction of LZTFL1 with the IFT-B complex (Eguether *et al.*, 2014). We recently showed that the interaction of IFT74–IFT81 with IFT25–IFT27 is crucial for BBSome-mediated GPCR export, as variations of IFT74/BBS22 and IFT27/BBS19 found in BBS patients impair this interaction and cause BBS-associated ciliary defects (Zhou *et al.*, 2022).

In addition to other IFT-B subunits, the IFT74–IFT81 heterodimer also interacts with the Rab-like small GTPase RABL2 (Figure 1, A and B); in this context, it is interesting to note that IFT22 and IFT27 are also Rab-like GTPases known as RABL5 and RABL4, respectively (Yan and Shen, 2022). Previous studies by us and others showed that RABL2 in its GTP-bound state interacts with the basal body protein CEP19 (Kanie *et al.*, 2017; Nishijima *et al.*, 2017). Intriguingly, mutations in *CEP19* and *RABL2* in humans and mice are known to lead to BBS-associated abnormalities (Shalata *et al.*, 2013; Lo *et al.*, 2016; Kanie *et al.*, 2017; Bölükbaşi *et al.*, 2018; Duan *et al.*, 2021). On the other hand, RABL2 was also suggested to regulate the targeting of ciliary GPCRs by directly binding to them (Dateyama *et al.*, 2019; Barbeito *et al.*, 2021). Furthermore, while this study was in progress, Duan *et al.* proposed a model in which RABL2 indirectly regulates BBSome-mediated GPCR export across the TZ via allosterically binding to the IFT-B complex (Duan *et al.*, 2021).

In the course of our previous study (Zhou *et al.*, 2022), we noticed that RABL2(Q80L), a GTP-locked mutant, and IFT25–IFT27 appear to bind to partially overlapping regions of the IFT74–IFT81 dimer (Figure 1B). We here extended our previous study and found that RABL2(Q80L) and IFT25–IFT27 bind to IFT74–IFT81 in a mutually exclusive manner, indicating that the binding of RABL2(Q80L) to IFT74–IFT81 decouples IFT25–IFT27 from IFT74–IFT81 and causes BBS-associated ciliary defects, such as abnormal accumulation of the BBSome and GPCRs within cilia.

RESULTS

RABL2(Q80L) and IFT25–IFT27 bind to an overlapping region of IFT74–IFT81 in a mutually exclusive manner

As summarized in Figure 1B, our previous study suggested that in the IFT74–IFT81 dimer, the binding region of the IFT25–IFT27 dimer overlaps with that for RABL2B(Q80L) [hereafter referred to as RABL2(Q80L); humans have two nearly identical RABL2 paralogs, RABL2A and RABL2B (Kramer *et al.*, 2010)]. We first confirmed our previous results by utilizing the visible immunoprecipitation (VIP) assay, which enables visual screening of one-to-many and many-to-many protein interactions, as well as binary interactions using fluorescent fusion proteins (Katoh *et al.*, 2015, 2016). However, the following points should be noted regarding the VIP assay: the expression levels and stability of individual proteins vary from protein to protein and may hence be affected by the coexpressed proteins, and interactions may be hampered by the fluorescent protein tags.

HEK293T cells were cotransfected with expression vectors for EGFP-IFT81, a TagBFP (tBFP)-fused IFT74 construct, and either mCherry (mChe)-fused RABL2(Q80L) or IFT25+IFT27, and lysates prepared from the transfected cells were processed for immunoprecipitation with glutathione *S*-transferase (GST)-fused anti-GFP nanobody (Nb) prebound to glutathione-Sepharose 4B beads. Observation of the precipitated beads bearing fluorescent fusion proteins under a microscope demonstrated blue-fluorescent signals for all the tBFP-IFT74 constructs analyzed (Supplemental Figure S1A, second row), indicating that IFT81 can form a dimer with all the IFT74 constructs. Red signals for RABL2(Q80L)-mChe were detected when tBFP-fused IFT74(WT) (Supplemental Figure S1A, column 1) or IFT74(1–526) (column 3) was coexpressed with EGFP-IFT81 and RABL2(Q80L)-mChe. By contrast, red signals were not detected when tBFP-IFT74(Δ421–485) was coexpressed (column 2), indicating that the region of IFT74 encompassing at least residues 421–485 contributes to RABL2(Q80L) binding (Figure 1B). When similar experiments were performed for mChe-fused IFT25+IFT27, red signals were detected for tBFP-fused IFT74(WT) (Supplemental Figure S1A, column 4) but not for IFT74(1–526) (column 6), indicating that the region comprising residues 527–600 of IFT74 contributes to its binding to IFT25–IFT27. On the other hand, red signals were decreased when tBFP-IFT74(Δ421–485) was coexpressed (column 5), suggesting that the IFT25–IFT27-binding region of IFT74 partially overlaps with the RABL2(Q80L)-binding region (Figure 1B).

When similar VIP analyses were performed using EGFP-IFT74 and tBFP-fused deletion constructs of IFT81 (Supplemental Figure S1B), the deletion of residues 448–502 and 556–593 of IFT81 abolished its binding to RABL2(Q80L) (column 2) and IFT25+IFT27 (column 6), respectively, and the deletion of residues 448–502 of IFT81 partially reduced its ability to bind IFT25+IFT27 (column 5). Taken together with the results shown in Supplemental Figure S1A, these results indicate that the relatively broad binding region of the IFT74–IFT81 dimer to the IFT25–IFT27 dimer partially overlaps with its RABL2(Q80L)-binding region (Figure 1B).

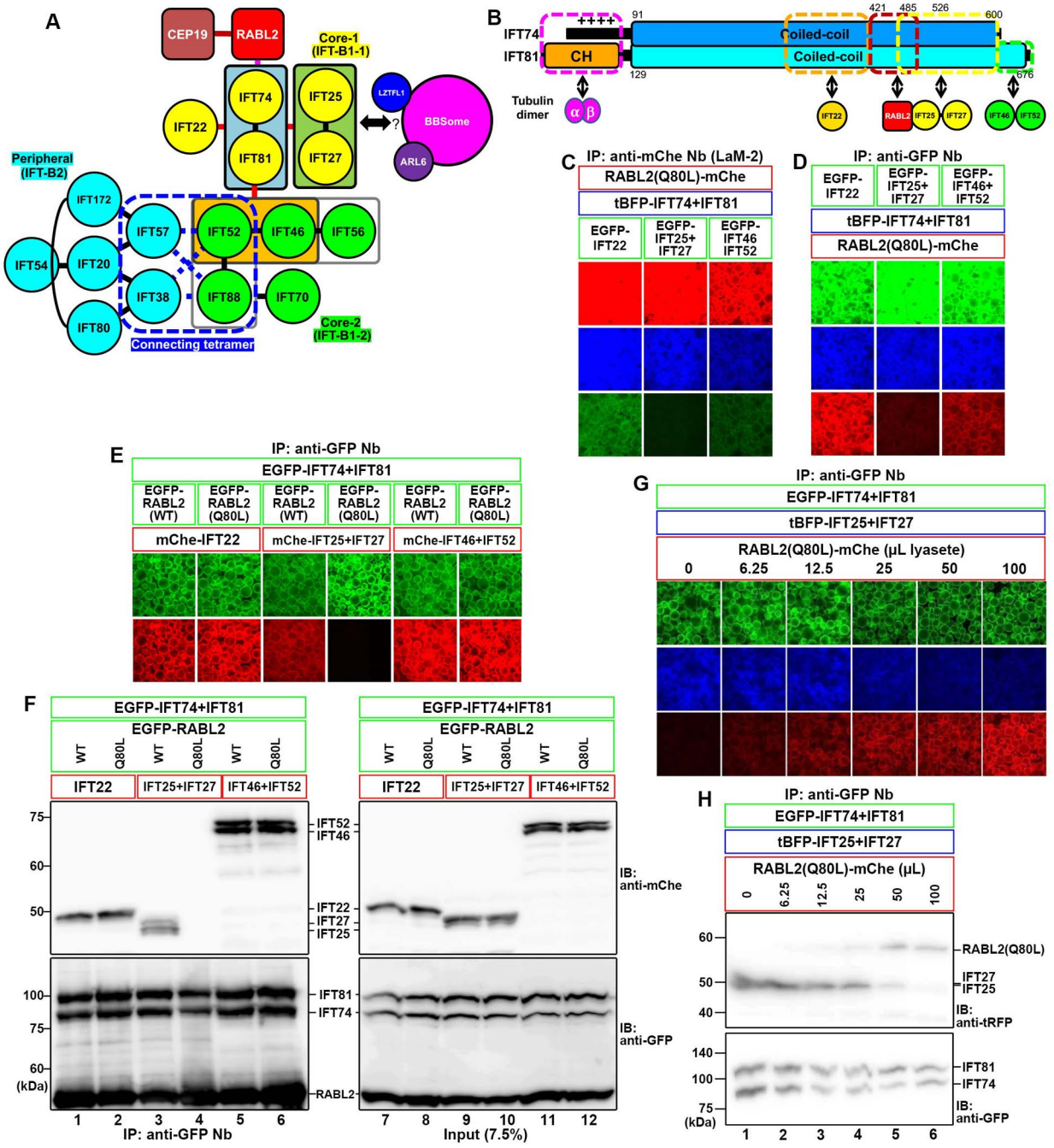

FIGURE 1: Mutually exclusive binding of RABL2(Q80L) and IFT25–IFT27 to IFT74–IFT81. (A) Overall architecture of the IFT-B complex and its interaction with RABL2 predicted from our previous studies (for a review, see Nakayama and Katoh [2020]). (B) Summary of the regions of the IFT74–IFT81 dimer responsible for its interactions with IFT22, RABL2(Q80L), IFT25–IFT27, and IFT46–IFT52, predicted from our previous study (Zhou *et al.*, 2022). CH, calponin-homology domain. (C, D) Lysates prepared from HEK293T cells cotransfected with expression vectors for RABL2(Q80L)-mChe, tBFP-fused IFT74+IFT81, and EGFP-fused IFT22, IFT25+IFT27, or IFT46+IFT52 were subjected to the VIP assay using GST-fused anti-mChe Nb (LaM-2 version) (C) or anti-GFP Nb (D) prebound to glutathione-Sepharose 4B beads. Note that anti-GFP Nb or anti-mChe Nb cannot react with tBFP as described previously (Satoda *et al.*, 2022; Zhou *et al.*, 2022). (E, F) Lysates prepared from cells coexpressing EGFP-fused IFT74+IFT81, either EGFP-fused RABL2(WT) or RABL2(Q80L) as indicated, and either mChe-fused IFT22, IFT25+IFT27, or IFT46+IFT52 as indicated were subjected to immunoprecipitation with GST-fused anti-GFP Nb prebound to glutathione-Sepharose 4B beads (E), followed by immunoblotting analysis with anti-mChe and anti-GFP antibodies (F). (G, H) Constant amounts of lysates (100 µl lysates) prepared from cells coexpressing EGFP-fused IFT74+IFT81 and tBFP-fused IFT25+IFT27 were mixed with varying amounts of lysates (0–100 µl lysates) from RABL2(Q80L)-mChe-expressing cells. The mixture was subjected to immunoprecipitation with GST-fused anti-GFP Nb prebound to glutathione-Sepharose 4B beads at 4°C for 4 h (G), followed by immunoblotting analysis using anti-tRFP antibody and anti-GFP antibodies (H); note that the anti-tRFP antibody, which recognizes tRFP-derived tBFP, cross-reacts with mChe as described previously (Funabashi *et al.*, 2018).

Mutually exclusive binding of RABL2(Q80L) and IFT25–IFT27 to IFT74–IFT81

Based on the above results, it is possible that RABL2(Q80L) and IFT25–IFT27 bind to an overlapping region of the IFT74–IFT81 dimer in a mutually exclusive manner. To address this possibility, mChe-fused RABL2(Q80L) and tBFP-fused IFT74+IFT81 were coexpressed with either EGFP-fused IFT22, or IFT25+IFT27, or IFT46+IFT52 in HEK293T cells, and lysates prepared from the cells were analyzed by the VIP assay using GST-tagged anti-mChe Nb (LaM-2 version) or anti-GFP Nb. As shown in Figure 1C, RABL2(Q80L)-mChe was able to coprecipitate EGFP-fused IFT22 and IFT46+IFT52 together with tBFP-fused IFT74+IFT81 (columns 1 and 3), indicating simultaneous interactions of IFT74–IFT81 with RABL2(Q80L) and either IFT22 or IFT46–IFT52. By contrast, the fluorescence of GFP-fused IFT25+IFT27 (column 2) coprecipitated with RABL2(Q80L)-mChe using anti-mChe Nb was much weaker than that of IFT22 and IFT46+IFT52, even in the presence of coexpressed tBFP-IFT74+IFT81. Reciprocally, the fluorescence of RABL2(Q80L)-mChe coprecipitated with EGFP-fused IFT25+IFT27 using anti-GFP Nb appeared to be weak, even in the presence of coexpressed tBFP-IFT74+IFT81 (Figure 1D, column 2). These results indicate that RABL2(Q80L) and IFT25–IFT27 bind to IFT74–IFT81 in a mutually exclusive manner, whereas the IFT74–IFT81 dimer can simultaneously bind to RABL2(Q80L) and either the IFT22 or the IFT46–IFT52 dimer.

To analyze whether the GTP-bound state of RABL2 is crucial for its mutually exclusive binding to IFT74–IFT81 with IFT25–IFT27, we then compared the binding of IFT74+IFT81 to IFT25+IFT27 in the presence of RABL2(WT) or RABL2(Q80L). To this end, EGFP-fused IFT74+IFT81 and mChe-fused IFT25+IFT27 were coexpressed together with EGFP-fused RABL2(WT) or RABL2(Q80L) in HEK293T cells, and lysates prepared from the cells were subjected to immunoprecipitation with anti-GFP Nb, followed by immunoblotting with anti-mChe and anti-GFP antibodies (Figure 1, E and F). The coprecipitation of IFT25+IFT27 with IFT74+IFT81 was almost completely abolished in the presence of coexpressed RABL2(Q80L) but not in the presence of RABL2(WT) (compare column 4 with column 3 in Figure 1E, and lane 4 with lane 3 in Figure 1F). The amounts of IFT22 and IFT46+IFT52 coprecipitated with IFT74+IFT81 were analyzed as controls and found to be comparable in the presence of coexpressed RABL2(WT) and RABL2(Q80L) (columns/lanes 1 and 2 and columns/lanes 5 and 6).

To further corroborate mutually exclusive binding of IFT25–IFT27 and RABL2(Q80L) to IFT74–IFT81, constant amounts of lysates of HEK293T cells coexpressing EGFP-fused IFT74+IFT81 and tBFP-fused IFT25+IFT27 were incubated with varying amounts of RABL2(Q80L)-mChe-expressing cell lysates and subjected to immunoprecipitation with anti-GFP Nb, followed by the VIP assay and immunoblotting analysis using anti-tRFP antibody. As shown in Figure 1G, the intensity of blue signals coimmunoprecipitated with anti-GFP-Nb was decreased, as the added amount of cell lysates expressing RABL2(Q80L)-mChe was increased. The VIP results were confirmed by immunoblotting analysis. As shown in Figure 1H, the intensity of the tBFP-IFT25+IFT27 bands was decreased as the intensity of the RABL2(Q80L)-mChe band was increased, indicating that IFT25–IFT27 on IFT74–IFT81 was replaced by RABL2(Q80L); note that the anti-tRFP antibody, which recognizes tRFP-derived tBFP, cross-reacted with mChe as described previously (Funabashi *et al.*, 2018). Thus we conclude that RABL2 in its GTP-bound form binds the IFT74–IFT81 dimer via a region partially overlapping with the IFT25–IFT27-binding region and can displace IFT25–IFT27 from IFT74–IFT81 in the IFT-B complex.

Expression of RABL2(Q80L) causes BBS-associated ciliary defects

While this study was in progress, Duan *et al.* proposed that RABL2 acts as a molecular switch to fine-tune Hh signaling, on the basis of their observations that the expression of Rabl2(Q80L) but not Rabl2(WT) inhibits BBSome exit from cilia, which thereby inhibits the export of GPR161 and Smoothened (SMO) to suppress Hh signaling, and that Rabl2(Q80L) knock-in mice phenocopy *Ift27*-knockout (KO) mice (Duan *et al.*, 2021). The accumulation of GPCRs within cilia in RABL2(Q80L)-expressing cells was also reported by Dateyama *et al.* (Dateyama *et al.*, 2019). In the model proposed by Duan *et al.*, GTP-bound RABL2 is required for binding of the IFT-B complex to the BBSome, and GTP hydrolysis on RABL2 is key to decoupling of the BBSome from the retrograde IFT machinery and to the outward passage of BBSome-bound cargo GPCRs across the TZ (Duan *et al.*, 2021).

We first confirmed the observations of previous studies. When expressed in human telomerase reverse transcriptase-immortalized retinal pigment epithelial 1 (hTERT-RPE1) cells, EGFP-fused RABL2(Q80L) was found mainly around the ciliary base, with a minor proportion around the tip and within cilia (Figure 2C). The localization of ciliary RABL2(Q80L) resembled that of the IFT-B subunit IFT88 (see Supplemental Figure S2C), suggesting persistent binding of RABL2(Q80L) to IFT-B within cilia. By contrast, EGFP-RABL2(WT) was not detectable within cilia (Figure 2B; also see Figure 2H). Consistent with the previous study (Duan *et al.*, 2021), the exogenous expression of EGFP-fused RABL2(WT) or RABL2(Q80L) did not affect the ciliary level of IFT88 (Supplemental Figure S2, A–C). Considering the direct interaction of RABL2(Q80L), but not RABL2(WT), with IFT74–IFT81 in place of IFT25–IFT27 (Figure 1, E and F), the most straightforward explanation for these observations is that RABL2(Q80L) is imported into cilia via its binding to the IFT-B complex (see Figure 7B).

We then analyzed the localization of LZTFL1/BBS17, as this protein was shown to be accumulated within cilia in *Ift27*-KO cells and was proposed to connect the IFT-B complex to the BBSome for the removal of ciliary membrane proteins (Eguether *et al.*, 2014; Mick *et al.*, 2015). In control RPE1 cells, LZTFL1 was not detected within cilia (Figure 2A) and remained undetectable within cilia when EGFP-RABL2(WT) was stably expressed (Figure 2B). In striking contrast, the stable expression of EGFP-RABL2(Q80L) in RPE1 cells caused a high level of accumulation of LZTFL1 within cilia (Figure 2C), as in *IFT27*-KO cells (Figure 2D; also see Figure 2I), which is in agreement with a previous study showing that LZTFL1 functions downstream of IFT25–IFT27 (Eguether *et al.*, 2014). The localization of IFT88 was confirmed not to be substantially changed in *IFT27*-KO cells compared with control cells (Supplemental Figure S2, A and D), consistent with previous studies (Eguether *et al.*, 2014; Mick *et al.*, 2015).

Similar results were obtained for the ciliary localizations of BBS9 and ARL6/BBS3; these proteins were found in approximately 20 to 30% of cilia in control RPE1 cells (Seo *et al.*, 2011; Nozaki *et al.*, 2018; Zhou *et al.*, 2022). The expression of EGFP-RABL2(WT) in RPE1 cells did not substantially alter the ciliary level of BBS9 (Figure 3, A and B) or ARL6 (Figure 3, H and I). By contrast, EGFP-RABL2(Q80L) expression caused significant enrichment of BBS9 (Figure 3C) and ARL6 (Figure 3J) within cilia, as in *IFT27*-KO cells (Figure 3, D and K; also see Figure 3, O and P).

We then analyzed the effects of RABL2(WT) or RABL2(Q80L) expression on changes in the ciliary localizations of the GPCRs GPR161 and SMO, which suppresses and activates the Hh signaling pathway, respectively (Anvarian *et al.*, 2019; Kopinke *et al.*, 2021). In control cells in the basal state, GPR161 is present on the ciliary membrane

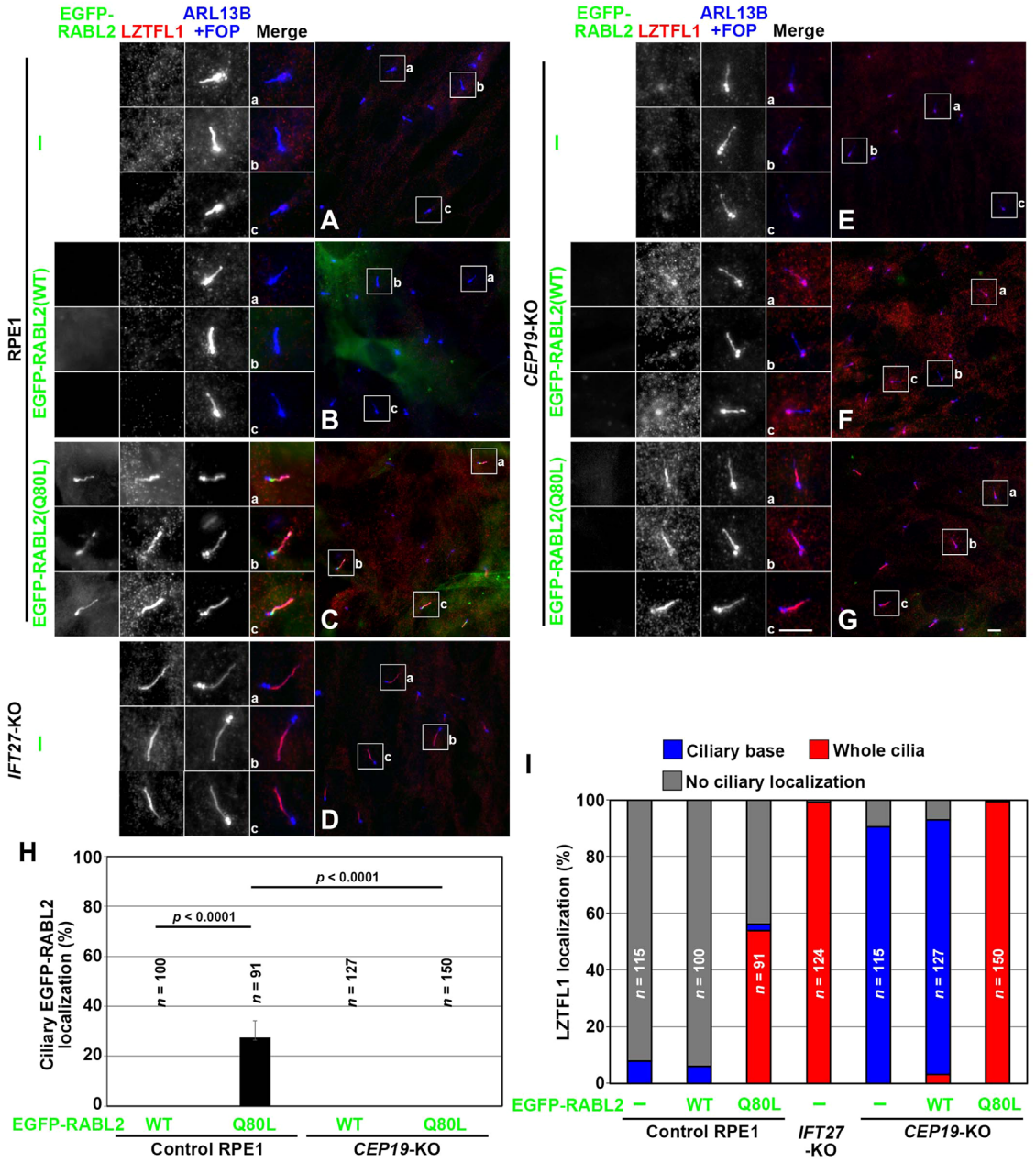

FIGURE 2: RABL2(Q80L) causes enrichment of LZTFL1 within cilia. (A–G) Control RPE1 cells (A–C), *IFT27*-KO cells (D), and *CEP19*-KO cells (#CEP19-1-12 cell line) (E–G) were left uninfected (A, D, E) or infected with a lentiviral vector for EGFP-fused RABL2(WT) (B, F) or RABL2(Q80L) (C, G) to stably express the RABL2 construct. Cells were cultured for 24 h under serum-starved conditions to induce ciliogenesis and immunostained for LZTFL1 and ARL13B+FOP. Images of the boxed regions enlarged by 2.5-fold are shown on the left side. Scale bars, 5 μm. (H) RPE1 cells or *CEP19*-KO cells with ciliary localization of EGFP-fused RABL2(WT) or RABL2(Q80L) were counted, and the percentages are shown as bar graphs. Values are means ± SD of three independent experiments. In each set of experiments, 18–55 cells were analyzed (*n*, the total number of cells analyzed). Statistical significances were calculated using one-way ANOVA followed by the Dunnett's multiple comparison test. (I) Localization of LZTFL1 in the same sets of experiments was classified as "whole ciliary," "ciliary base," and "no ciliary localization," and the number of cells in each category was counted. The percentages of these categories are expressed as stacked bar graphs.

(Figure 4A), whereas SMO is excluded from cilia (Figure 5A). When the Hh pathway is stimulated by the treatment of cells with SMO Agonist (SAG), GPR161 exits cilia (Figure 4H), whereas SMO enters cilia (Figure 5H). In *IFT27*-KO cells, GPR161 (Figure 4, D and K) and SMO (Figure 5, D and K) were found at substantially high levels within cilia even under SAG-stimulated conditions and basal conditions, respectively (also see Figures 4O and 5O), probably due to the impaired export of these GPCRs across the TZ by decoupling of the cargo-loaded BBSome from the retrograde IFT machinery in the absence of IFT27. In RPE1 cells stably expressing RABL2(WT), changes in the ciliary localizations of GPR161 and SMO in response to SAG treatment were essentially the same as those observed in control RPE1 cells (Figures 4, B and I, and 5, B and I). In clear contrast, substantial levels of ciliary GPR161 (Figure 4, C and J) and

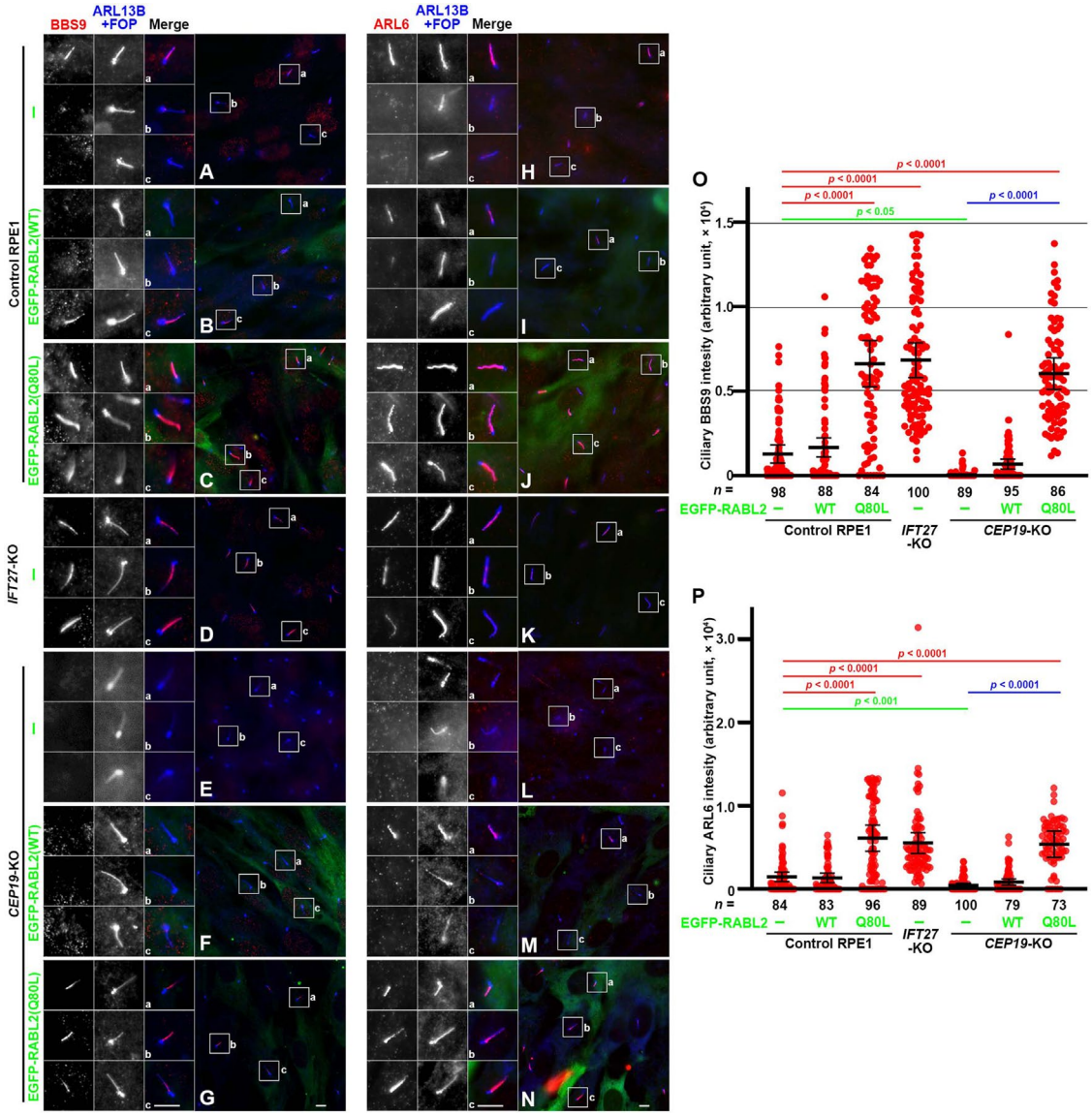

FIGURE 3: RABL2(Q80L) causes enrichment of BBS9 and ARL6 within cilia. (A–N) Control RPE1 cells (A–C, H–J), *IFT27*-KO cells (D, K), and *CEP19*-KO cells (#CEP19-1-12 cell line) (E–G, L–N) were left uninfected (A, D, E, H, K, L) or infected with a lentiviral vector for EGFP-fused RABL2(WT) (B, F, I, M) or RABL2(Q80L) (C, G, J, N) to stably express the RABL2 construct. The cells were serum-deprived for 24 h and immunostained for either BBS9 (A–G) or ARL6 (H–N) and ARL13B+FOP. Images of the boxed regions enlarged by 2.5-fold are shown on the left side. Scale bars, 5 μm. Note that the ciliary localization of EGFP-RABL2(Q80L) could not be detected under the fixation/permeabilization conditions used in these experiments. (O, P) The ciliary staining intensities for BBS9 (O) or ARL6 (P) were measured and expressed as scatter plots. Dots indicate individual samples. Values are shown as means ± SD. Statistical significances were calculated using one-way ANOVA followed by the Dunnett's multiple comparison test.

SMO (Figure 5, C and J) were detectable even under SAG-stimulated conditions and basal conditions, respectively, in RABL2(Q80L)-expressing RPE1 cells, as in *IFT27*-KO cells (see Figures 4O and 5O).

Thus these observations can all be explained if RABL2(Q80L) displaces IFT25–IFT27 from IFT74–IFT81 in the IFT-B complex, resulting in decoupling of the BBSome from the IFT-B complex (see Figure 7B).

RABL2(Q80L) requires CEP19 for its ciliary entry but not for its ability to induce ciliary accumulation of LZTFL1 and the BBSome

We previously showed that the basal body protein CEP19 and IFT74–IFT81 bind to RABL2(Q80L) in a mutually exclusive manner (Nishijima *et al.*, 2017). At about the same time, Kanie *et al.* proposed a model in which CEP19 captures activated RABL2 at the basal body, and RABL2 in turn captures and releases the IFT-B complex to initiate entry of the IFT machinery into cilia (Kanie *et al.*, 2017); consistent with this proposal, *CEP19*-KO cells were mildly compromised with respect to ciliogenesis compared with control RPE1 cells (Supplemental Figure S3A), as described previously (Nishijima *et al.*, 2017). In addition, Kanie *et al.* reported that the ciliogenesis defect of *CEP19*-KO cells was rescued by overexpression of RABL2(Q80L) and partially by that of RABL2(WT) (Kanie *et al.*, 2017), although our analysis showed that the mild ciliogenesis defect of *CEP19*-KO cells was partially rescued by exogenous expression of both RABL2(WT) and RABL2(Q80L) (Supplemental

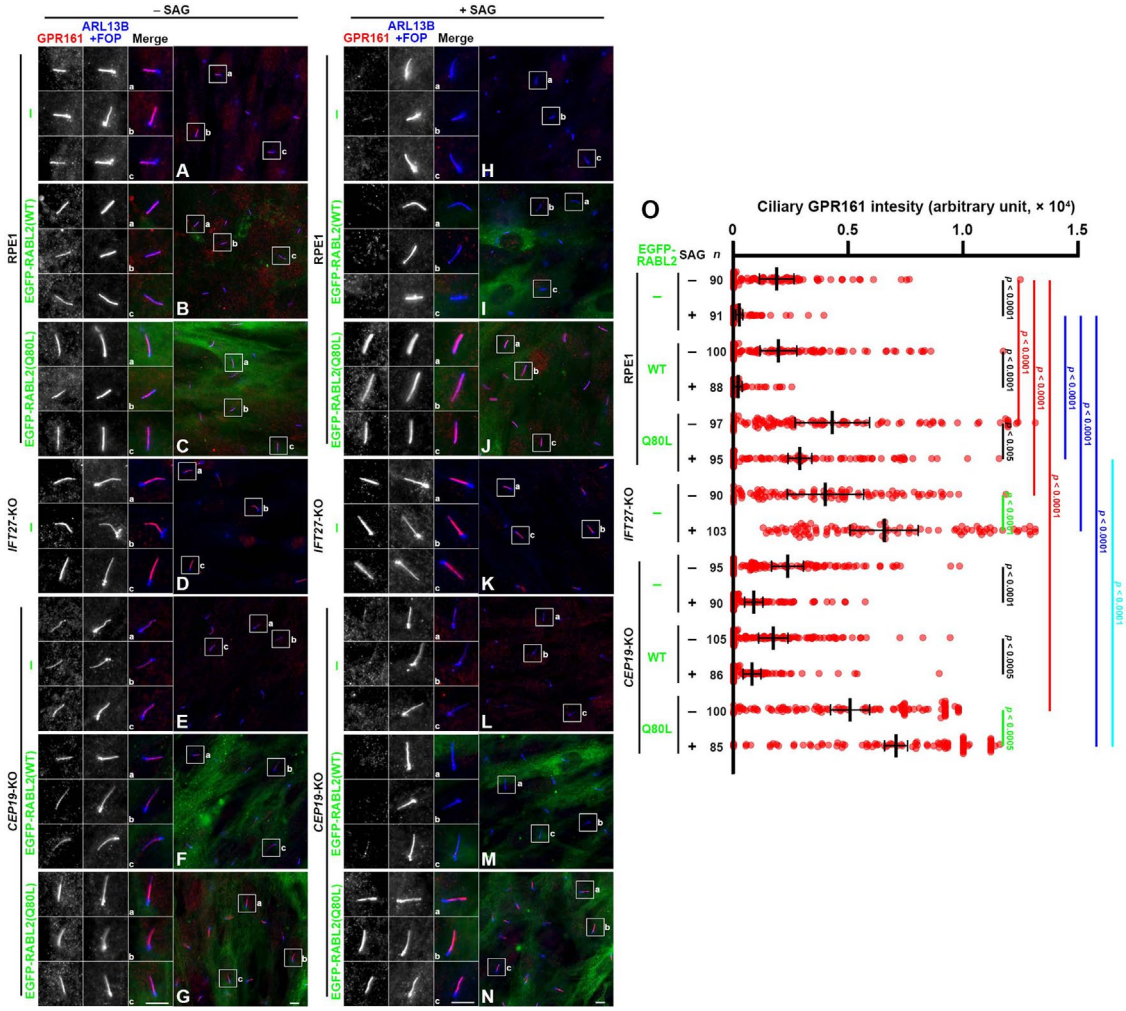

FIGURE 4: RABL2(Q80L) suppresses the export of GPR161 from cilia via Hh pathway activation. (A–N) Control RPE1 cells (A–C, H–J), *IFT27*-KO cells (D, K), and *CEP19*-KO cells (#CEP19-1-12 cell line) (E–G, L–N) were left uninfected (A, D, E, H, K, L) or infected with a lentiviral vector for EGFP-fused RABL2(WT) (B, F, I, M) or RABL2(Q80L) (C, G, J, N) to stably express the RABL2 construct. Cells were serum-deprived for 24 h and further incubated for 24 h in the presence (+SAG) or absence (–SAG) of 200 nM SAG. The cells were immunostained with antibodies against either GPR161 and ARL13B+FOP. Scale bars, 5 μm. (O) Relative ciliary staining intensities of GPR161were estimated and expressed as scatter plots. Dots indicate individual samples. Horizontal lines and error bars are means and SD, respectively. Total numbers of analyzed cells are shown (*n*). Statistical significances were calculated using one-way ANOVA followed by the Dunnett's multiple comparison test.

Figure S3A). We therefore analyzed the localization of EGFP-fused RABL2(WT) and RABL2(Q80L) in *CEP19*-KO cells (the #CEP19-1-12 cell line) (Nishijima *et al.*, 2017). As in control RPE1 cells (Figure 2B), EGFP-RABL2(WT) was not detected at the ciliary base or within cilia in *CEP19*-KO cells (Figure 2F). EGFP- RABL2(Q80L) was also undetectable at the ciliary base and within cilia in *CEP19*-KO cells (Figure 2G; also see Figure 2H). This was somewhat unexpected because Kanie *et al.* reported that GFP-RABL2(Q80L) was found at the ciliary base and within cilia in *CEP19*-KO RPE1 cells (Kanie *et al.*, 2017). To exclude the possibility that the failure of the ciliary localization of RABL2(Q80L) in our *CEP19*-KO cells was a cell line-dependent observation, we expressed EGFP-RABL2(Q80L) in another *CEP19*-KO cell line, #CEP19-1-2 (Nishijima *et al.*, 2017). However, the ciliary localization of EGFP-RABL2(Q80L) was not detectable in either the #CEP19-1-2 or the #CEP19-1-12 cell line (Supplemental Figure S3, C and D). Although the exact reason for the difference between our observations and those of Kanie *et al.* (2017) is unclear, it is possible that the observations differed because of the different gRNAs used and their target sequences; our gRNA targeted a sequence in exon 2, while that of Kanie *et al.* targeted an exon 3 sequence. In the previous study, we experienced that even KOs of the same gene can lead to subtle differences in the phenotype of the KO cells due to differences in the position of the indel and thus in the resulting truncated protein (Tsurumi *et al.*, 2019). Another possibility is that RABL2(Q80L) is moving in and out across the TZ by diffusion and we failed to detect it. Nevertheless, our observations suggest that efficient entry of RABL2(Q80L) across the TZ, probably via binding to anterograde IFT trains, requires its prior interaction with CEP19 at the basal body (see *Discussion*).

We then analyzed the localization of LZTFL1 in *CEP19*-KO cells and in those cells expressing EGFP-fused RABL2(WT) or RABL2(Q80L). Unexpectedly, in *CEP19*-KO cells and in those cells expressing RABL2(WT), LZTFL1 was found enriched around the ciliary base (Figure 2, E and F; also see Figure 2P); this will be discussed later (see *Discussion*). When RABL2(Q80L) was expressed in *CEP19*-KO cells, LZTFL1 was found to substantially accumulate within cilia (Figure 2G;

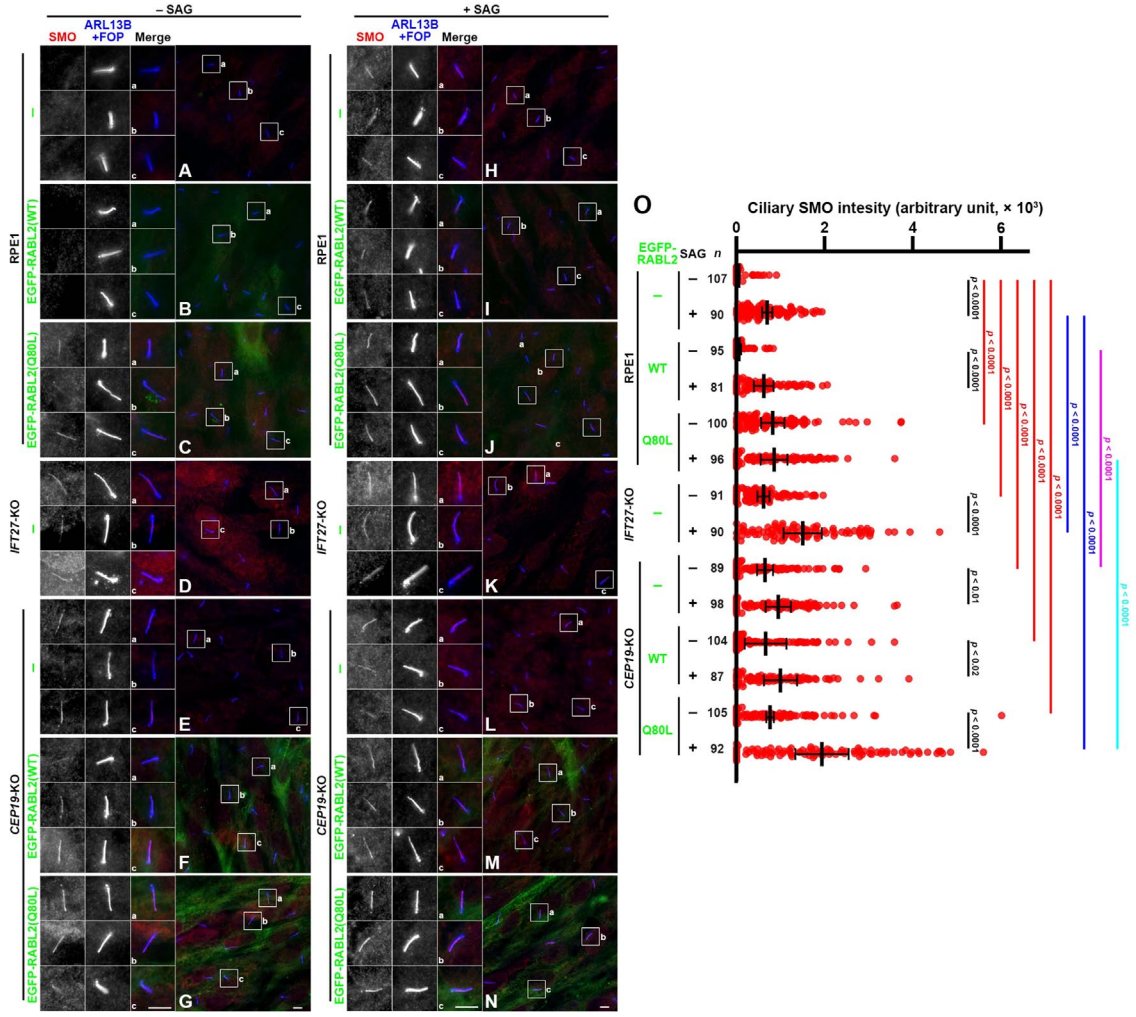

FIGURE 5: RABL2(Q80L) suppresses basal SMO export from cilia. (A–N) Control RPE1 cells (A–C, H–J), *IFT27*-KO cells (D, K), and *CEP19*-KO cells (#CEP19-1-12 cell line) (E–G, L–N) were left uninfected (A, D, E, H, K, L), or infected with a lentiviral vector for EGFP-fused RABL2(WT) (B, F, I, M) or RABL2(Q80L) (C, G, J, N) to stably express the RABL2 construct. The cells were treated as described in the legend for Figure 4, A–N, and immunostained with antibodies against either SMO or ARL13B+FOP. Scale bars, 5 μm. (O) Relative ciliary staining intensities of SMO were estimated and expressed as scatter plots as described in the legend for Figure 4O.

also see Figure 2P) as in control RPE1 cells, even though RABL2(Q80L) itself was not found within cilia (Figure 2G). We also analyzed the localizations of BBS9 and ARL6. Like LZTFL1, both BBS9 and ARL6 were enriched within cilia in *CEP19*-KO cells expressing EGFP-RABL2(Q80L) to a greater extent than in those cells with or without the expression of EGFP-RABL2(WT) (Figure 3, E–G and L–N; also see Figure 3 O and P). These results suggest that RABL2(Q80L) causes the ciliary accumulation of LZTFL1, BBS9, and ARL6, regardless of its constant localization within cilia.

It is noteworthy that the ciliary levels of BBS9 and ARL6 were significantly lower in *CEP19*-KO cells than in control RPE1 cells (compare Figure 3E with Figure 3, A and L and with Figure 3H; also see Figure 3, O and P). This is in line with the previous proposal that CEP19 is involved not only in the recruitment of but also in the activation of RABL2, and that the GTP-locked form of RABL2 can bypass the requirement for CEP19 (Kanie *et al.*, 2017) (see *Discussion*).

We then analyzed the effect of RABL2(Q80L) expression on the localizations of GPR161 and SMO in *CEP19*-KO cells under basal and SAG-stimulated conditions. As in control RPE1 cells (Figure 4, C and J), the expression of EGFP-RABL2(Q80L) in *CEP19*-KO cells inhibited the exit of GPR161 from cilia upon SAG stimulation (Figure 4, G and N) and increased the basal ciliary SMO level (Figure 5G) compared with the expression of EGFP-RABL2(WT) (Figures 4, F and M, and 5F; also see Figures 4O and 5O). Thus RABL2(Q80L) can inhibit the exit of ciliary GPCRs even in the absence of CEP19. It is also interesting to note that, even in the absence of exogenous RABL2(Q80L) expression, the basal ciliary SMO level was significantly higher in *CEP19*-KO cells than in control cells (compare Figure 5E with Figure 5A; also see Figure 5O) and that GPR161 within cilia also tended to be maintained at higher levels in *CEP19*-KO cells than in control cells after SAG treatment (Figure 4O). The high ciliary levels of SMO and GPR161 in *CEP19*-KO cells may be associated with the low ciliary levels of BBS9 and ARL6 (Figure 3, O and P) (see *Discussion*).

Coprecipitation of IFT-B subunits with EGFP-RABL2(Q80L)

Duan *et al.* (2021) presented data indicating that EGFP-Rabl2(Q80L) can coprecipitate IFT25 as well as other IFT-B subunits, such as IFT81 and IFT52 (Duan *et al.*, 2021). This was apparently inconsistent with our data indicating that the IFT25–IFT27 dimer and

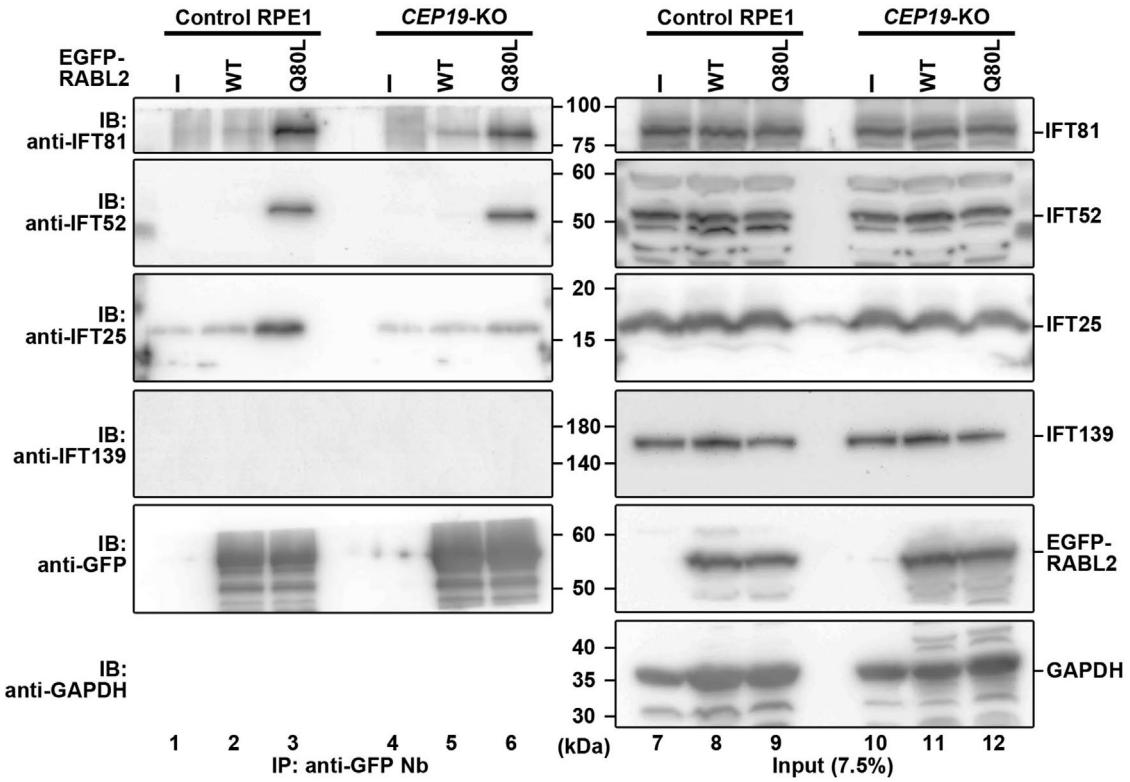

FIGURE 6: Coprecipitation of IFT-B subunits with RABL2(Q80L). Lysates were prepared from RPE1 cells or *CEP19*-KO cells (#CEP19-1-12 cell line), or those stably expressing EGFP-fused RABL2(WT) or RABL2(Q80L) as indicated and processed for immunoprecipitation using GST-tagged anti-GFP Nb. The precipitates were then subjected to SDS–PAGE and immunoblotting analysis using antibodies against IFT81, IFT52, IFT25, IFT139, GFP, and GAPDH.

RABL2(Q80L) bind to IFT74–IFT81 in a mutually exclusive manner. We therefore analyzed whether EGFP-RABL2(Q80L) can coprecipitate IFT25 together with other IFT-B subunits.

When lysates prepared from RPE1 cells expressing EGFP-fused RABL2(WT) or RABL2(Q80L) were processed for immunoprecipitation using anti-GFP Nb followed by immunoblotting analyses using antibodies against IFT-B subunits, RABL2(Q80L), but not RABL2(WT), was shown to coprecipitate endogenous IFT81 and IFT52 (Figure 6, top and second panels, lanes 2 and 3), indicating the association of RABL2(Q80L) with the IFT-B complex. In agreement with the results of Duan *et al.* (2021), IFT25 also coprecipitated with RABL2(Q80L) but not with RABL2(WT) (third panel, lanes 2 and 3). We then performed similar experiments using *CEP19*-KO cells expressing EGFP-fused RABL2(WT) or RABL2(Q80L). Compared with control RPE1 cells, the amount of IFT25 coprecipitated with EGFP-RABL2(Q80L) was substantially reduced in *CEP19*-KO cells (Figure 6, third panel, lanes 3 and 6), whereas comparable amounts of IFT81 and IFT52 were coprecipitated with RABL2(Q80L) in control and *CEP19*-KO cells (Figure 6, top and second panels, lanes 3 and 6). On the other hand, coprecipitation of IFT139, an IFT-A subunit, with RABL2(Q80L) was not detectable in control RPE1 cells or in *CEP19*-KO cells (Figure 6, fourth panel, lanes 3 and 6), consistent with the previous study (Duan *et al.*, 2021); even if the IFT-A and IFT-B complexes form IFT trains within cilia, the IFT-A and IFT-B complexes might weakly bind each other and easily dissociate into two complexes upon membrane rupture (Cole *et al.*, 1998; Mencarelli *et al.*, 2013). We hence speculate that the difference in the coprecipitation of IFT25 with RABL2(Q80L) between control RPE1 and *CEP19*-KO cells is attributable to the difference in the loading efficiency of the IFT25–IFT27 dimer at the ciliary base onto the assembling anterograde IFT trains containing multiple IFT-B units, rather than a single IFT-B complex (see *Discussion*).

DISCUSSION

By expanding on our earlier study (Zhou *et al.*, 2022), we showed here that the IFT25–IFT27 dimer and RABL2(Q80L) bind to overlapping regions of the IFT74–IFT81 dimer in a mutually exclusive manner (Figure 1) and found that RPE1 cells stably expressing RABL2(Q80L) (Figure 7B) phenocopy *IFT27*-KO cells (Figure 7E); the BBSome and LZTFL1/BBS17 are accumulated within cilia and BBSome-mediated removal of ciliary GPCRs is impaired, although the abnormal phenotypes appeared to be milder in RABL2(Q80L)-expressing cells than in *IFT27*-KO cells. Duan *et al.* proposed that RABL2(Q80L) weakens the association of IFT-B with the BBSome by inducing conformational changes in IFT27 (Duan *et al.*, 2021). However, as RABL2(Q80L) does not directly interact with IFT25–IFT27 (Figure 1, E and F), and the IFT25–IFT27 dimer constitutes the interface between the IFT-B complex and the BBSome (see Figure 1A) (Eguether *et al.*, 2014; Liew *et al.*, 2014), the results of the present study indicate that binding of RABL2(Q80L) to IFT74–IFT81 displaces the majority of IFT25–IFT27 from the IFT-B complex, thereby resulting in impairment of GPCR removal from cilia mediated by the BBSome together with IFT-B (Figure 7B).

It is noteworthy that *Rabl2*-KO and *Rabl2*-mutant mice develop adult-onset obesity, retinal degeneration, polydactyly, steatosis, and diabetes, which are symptoms reminiscent of BBS (Lo *et al.*, 2016; Kanie *et al.*, 2017; Duan *et al.*, 2021), and that nonsense mutations in CEP19, which links RABL2 to the basal body protein FOP/CEP43

(Kanie *et al.*, 2017; Nishijima *et al.*, 2017), are also known to cause BBS-associated abnormalities (Shalata *et al.*, 2013; Bölükbaşi *et al.*, 2018). Although the exact mechanism underlying the cellular defects caused by these mutations is unknown, the lack of functional CEP19 might affect the activation/inactivation of RABL2 or the balance of RABL2 distribution among the cell body, the ciliary base, and cilia (Kanie *et al.*, 2017). Consistent with this speculation, RABL2(Q80L) caused accumulation of the BBSome and LZTFL1 within cilia and impaired GPCR removal from cilia even in *CEP19*-KO cells, suggesting that GTP-locked RABL2 can bypass the requirement of CEP19 for its function, although ciliary entry of GTP-bound RABL2 across the TZ requires CEP19 at the basal body (Figure 7D). The result that, unlike in control RPE1 cells, RABL2(Q80L) was not detectable within cilia in *CEP19*-KO cells is intuitively incompatible with the model of Duan *et al.* wherein GTP hydrolysis on RABL2 resulting in its dissociation from retrograde trains occurs on the distal side of the TZ (namely, within cilia) and is required for outward passage of the BBSome and its cargoes across the TZ (Duan *et al.*, 2021; Yan and Shen, 2022). Although the data presented here do not completely exclude the model proposed by Duan *et al.*, we favor the model that RABL2 in its GTP-bound form enables the efficient recruitment of the IFT-B complex to the ciliary base to promote assembly of anterograde trains (Figure 7, A and B; also see the legend for Figure 7A) as proposed by Kanie *et al.* (2017) (see below).

Superresolution imaging analyses by us and others demonstrated two distinct pools of IFT proteins at the ciliary base (Yang *et al.*, 2015, 2019; Katoh *et al.*, 2020). One pool is in the distal appendage (DA) region of the basal body where IFT proteins may be recruited from the cell body, and the other is on the distal side of the TZ and may be derived from the retrograde IFT trains and act as a waiting station where IFT components from retrograde trains and from the DA pool can be mixed (Nakayama and Katoh, 2020). It is also interesting to note a recent in situ cryoelectron tomographic (cryo-ET) study of assembling anterograde IFT trains at the ciliary base (van den Hoek *et al.*, 2022), in addition to cryo-ET studies of mature anterograde trains of *Chlamydomonas* and mammals (Jordan *et al.*, 2018; Kiesel *et al.*, 2020). The cryo-ET structures support the mechanism of the stepwise assembly of anterograde trains on the cytoplasmic side of the TZ before ciliary entry; the trains that are being assembled always contain a series of IFT-B units (estimated to contain an average of 62 IFT-B units in anterograde trains) (van den Hoek *et al.*, 2022), and subsequently IFT-A and IFT dynein are added to the IFT-B backbone scaffold. In view of the previous *Chlamydomonas* studies showing that IFT25–IFT27 dimers are predominantly present in a free form in the cell body (Wang *et al.*, 2009) and recruited to the IFT-B pool at the basal body from the cell body (Wingfield *et al.*, 2017), in conjunction with the localizations of CEP19 and FOP/CEP43 to the basal body, it is possible that RABL2 in its GTP-bound form promotes the recruitment of the IFT-B complex lacking IFT25–IFT27 to the basal body region via binding to IFT74–IFT81 and after hydrolysis of bound GTP is replaced with the IFT25–IFT27 dimer (Figure 7A). Although we were unable to detect EGFP-RABL2(WT) within cilia, high sensitivity live imaging previously demonstrated anterograde and less frequent retrograde movements of 3× mNeonGreen-tagged Rabl2-positive puncta within cilia (Duan *et al.*, 2021). Considering that individual anterograde IFT trains contain multiple IFT-B units (Jordan *et al.*, 2018; van den Hoek *et al.*, 2022), it is likely that a proportion of RABL2, probably in its GTP-bound state, can enter cilia across the TZ via continuous binding to a minor fraction of the IFT-B units in anterograde trains in place of IFT25–IFT27 (Figure 7A). On the other hand, IFT25–IFT27 is likely to be loaded onto a minor fraction of the IFT-B units in individual assembling trains even in the presence of RABL2(Q80L) persistently bound to other IFT-B units (Figure 7B), because IFT25, together with other IFT-B subunits, was coprecipitated with RABL2(Q80L) in control RPE1 cells (Figure 6, lane 3) (Duan *et al.*, 2021) and less efficiently in *CEP19*-KO cells (Figure 6, lane 6), even though IFT25–IFT27 and RABL2(Q80L) bind to IFT74–IFT81 in a mutually exclusive manner (Figure 1, E and F). Although at present it remains unclear whether IFT25–IFT27 is incorporated into IFT trains in *CEP19*-KO cells and those cells expressing RABL2(WT), we expect that a minor proportion of RABL2(WT) can be activated even in the absence of CEP19 and mediate loading of the IFT25–IFT27 dimer onto the anterograde trains (Figure 7C), as RABL2 can bind to GTP via its intrinsic guanine nucleotide exchange activity (Kanie *et al.*, 2017). Our attempts to establish *RABL2*-KO cells from hTERT-RPE1 cells have been unsuccessful to date, as humans have two closely related RABL2 paralogs, RABL2A and RABL2B (Kramer *et al.*, 2010). Detailed comparisons of the phenotypes of *RABL2*-KO and *CEP19*-KO cells will be helpful to understand the role of RABL2 in the regulation of ciliary protein trafficking involving the IFT machinery and the BBSome.

Apparently inconsistent with the roles of RABL2 suggested by Duan *et al.* (2021) and in this study, Dateyama *et al.* (2019) proposed a model in which GTP-bound RABL2 promotes the loading of GPR161 onto the IFT machinery at the ciliary base and thereby its entry into cilia via a direct interaction (Dateyama *et al.*, 2019). However, they analyzed the localization of GPR161 only in the basal state and did not analyze its removal from cilia upon Hh pathway stimulation. Furthermore, they presented data indicating that RABL2 interacts with GPR161 independently of its guanine nucleotide-binding state. Further experiments will be needed to validate this model.

One unexpected observation in this study was the localization of LZTFL1 around the ciliary base in *CEP19*-KO cells, whereas its distinct localization around the ciliary base or within cilia was not detected in control RPE1 cells (compare Figure 2E with Figure 2A). LZTFL1 was proposed to bridge the BBSome to the IFT-B complex (Eguether *et al.*, 2014); however, LZTFL1 has been reported to directly interact with only the BBSome, and not with IFT-B (Seo *et al.*, 2011; Sun *et al.*, 2021). A recent study in *Chlamydomonas* suggested that LZTFL1 controls BBSome recruitment to the basal body for its entry into cilia (Sun *et al.*, 2021). This is apparently inconsistent with the observations in mammalian cells that the BBSome accumulates within cilia in the absence of LZTFL1 (Seo *et al.*, 2011; Eguether *et al.*, 2014; Jiang *et al.*, 2016). On the other hand, our data showed that the ciliary levels of the BBSome and ARL6 are decreased in *CEP19*-KO cells (Figure 3, E, O, L, and P). In view of the previous study indicating that the BBSome can enter cilia independently of IFT27 (Liew *et al.*, 2014), LZTFL1 might be involved in BBSome entry into cilia in some way, in addition to the BBSome-mediated exit of ciliary GPCRs.

We previously showed the direct interaction of IFT38 with the BBSome utilizing the VIP assay (Nozaki *et al.*, 2019); the interaction was recently confirmed using purified BBSome (Yang *et al.*, 2020). We further showed that impairment of the IFT38–BBSome interaction results in inhibition of GPR161 export (Nozaki *et al.*, 2019). Intriguingly, however, in *IFT38*-KO cells expressing an IFT38 mutant defective in BBSome binding, the ciliary BBS9 or ARL6 level was not significantly changed, and SMO was not significantly enriched within cilia under basal conditions (Nozaki *et al.*, 2019), unlike in *IFT27*-KO cells (Figures 3 and 5) and in *BBS1*-KO cells (Nozaki *et al.*, 2018). Moreover, our analyses to date have not shown a direct interaction of IFT38 with IFT25–IFT27 or IFT74–IFT81 within the IFT-B complex (see Figure 1A). It is therefore likely that IFT25–IFT27 and

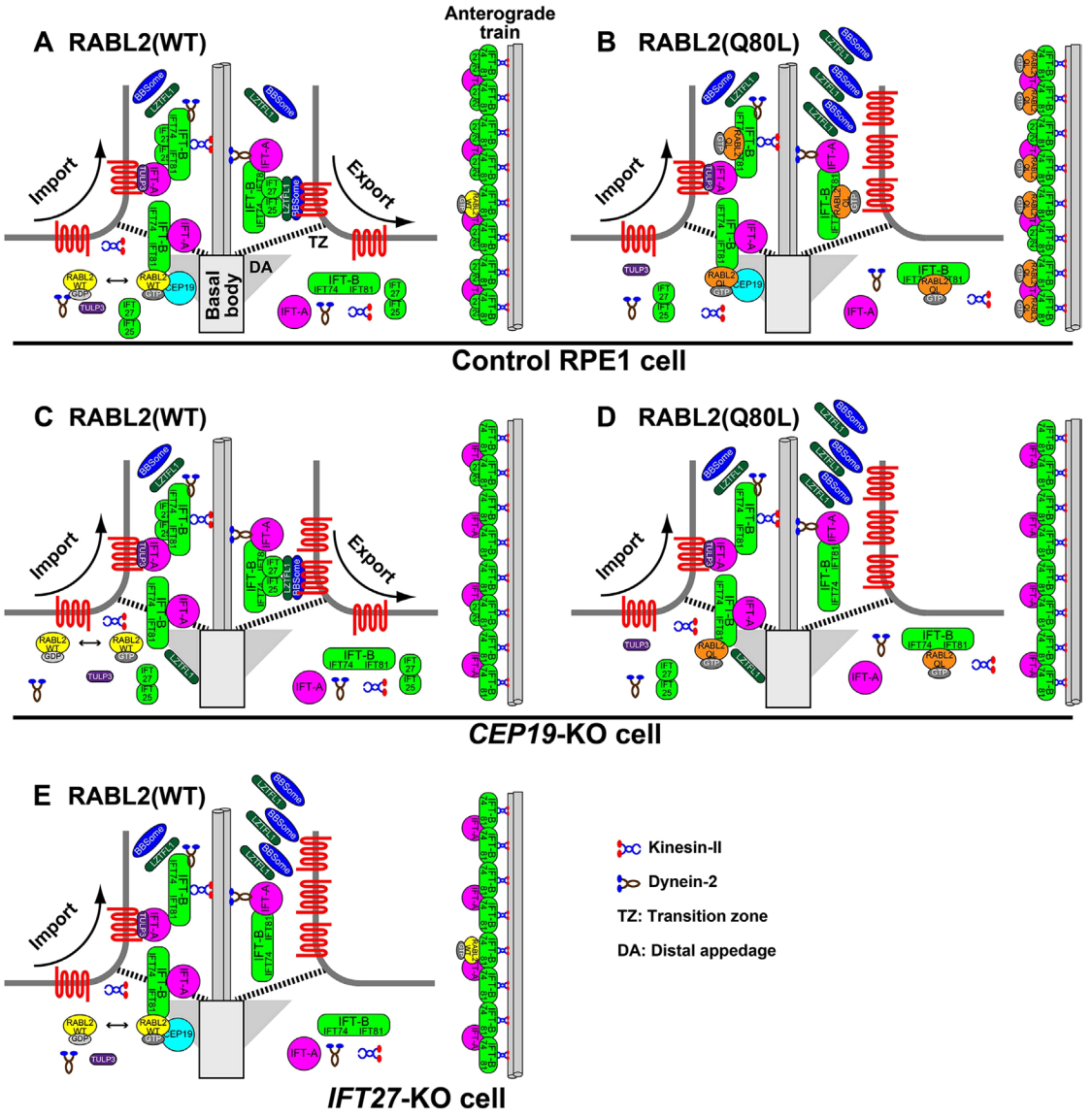

FIGURE 7: Models of mutually exclusive interactions of IFT25–IFT27 and RABL2(Q80L) with the IFT-B complex and their incorporation into IFT trains in control, *CEP19*-KO, and *IFT27*-KO cells. (A) Control RPE1 cells expressing RABL2(WT). After intrinsic nucleotide exchange of GDP for GTP (Kanie *et al.*, 2017), RABL2 is recruited to the ciliary base via interacting with CEP19 to promote subsequent recruitment of the IFT-B complex, which lacks IFT25–IFT27. The majority of RABL2 on IFT-B is then replaced by IFT25–IFT27 upon hydrolysis of bound GTP, although a fraction of RABL2 is likely to remain associated with some IFT-B units in the assembling train and enter cilia (Duan *et al.*, 2021). As the IFT-B units are linked, the IFT-A complex is recruited to the assembling train (van den Hoek *et al.*, 2022). The IFT train containing multiple IFT-B and IFT-A complexes then enters cilia across the TZ; a recent cryo-ET study of *Chlamydomonas* IFT trains suggested that mature anterograde trains contain an average of 62 IFT-B units (van den Hoek *et al.*, 2022). In parallel with the IFT entry, import of GPCRs across the TZ is mediated by the TULP3 adaptor bound to IFT-A. After transportation of the train along the axoneme driven by heterotrimeric kinesin-II and remodeling of the IFT train and motor exchange at the ciliary tip (not shown here), retrograde trafficking of the IFT machinery is driven by the dynein-2 complex. Finally, export of GPCRs across the TZ is mediated by the BBSome bound to the IFT-B complex. LZTFL1 somehow connects the BBSome to IFT25–IFT27. (B) Control RPE1 cells expressing RABL2(Q80L). The majority of RABL2(Q80L) is transported within cilia while continuing to associate with IFT-B without being replaced by IFT25–IFT27 (Duan *et al.*, 2021). As the majority of the IFT-B complex in the IFT train lacks IFT25–IFT27, the BBSome and LZTFL1 are unable to connect IFT-B to GPCRs and thereby unable to mediate their export across the TZ. Consequently, the BBSome and LZTFL1 are accumulated within cilia. (C) *CEP19*-KO cells expressing RABL2(WT). In the absence of CEP19 at the basal body, RABL2 is likely to less efficiently promote IFT-B assembly and mediate loading of IFT25–IFT27 onto IFT-B, although less efficiently. Export of GPCRs can partially occur, probably because some of the IFT-B units in the train contain IFT25–IFT27. (D) *CEP19*-KO cells expressing RABL2(Q80L). In the absence of CEP19, RABL2(Q80L) somehow prevents loading of IFT25-IFT27 onto IFT-B, even though it cannot itself enter cilia. As IFT-B lacks IFT25–IFT27, the BBSome and LZTFL1 are unable to connect GPCRs to IFT-B. (E) *IFT27*-KO cells expressing RABL2(WT). For lack of IFT25–IFT27, the BBSome and LZTFL1 are unable to connect IFT-B to GPCRs. For A and E, although we did not demonstrate entry of RABL2(WT) into cilia, its entry is likely to occur, albeit at a low level, on the basis of the data shown by Duan *et al.* (2021).

IFT38 are involved in BBSome-mediated GPCR export by distinct mechanisms. In this context, it is noteworthy that BBS is also caused by mutations in *IFT172*/*BBS20* (Bujakowska *et al.*, 2015; Schaefer *et al.*, 2016; Hirano *et al.*, 2020), which is a component of the IFT-B peripheral (IFT-B2) subcomplex together with IFT38. Although we did not detect a direct interaction between IFT38 and IFT172, it is possible that these two subunits have some effect on each other within the subcomplex to control the functions of the BBSome.

MATERIALS AND METHODS

Request a protocol through *Bio-protocol*.

Antibodies, chemicals, plasmids, and cell lines

Antibodies, chemicals, and plasmids used in this study are listed in Supplemental Table S1. HEK293T cells (RBC2202; RIKEN BioResource Research Center) were cultured in DMEM with high glucose (Nacalai Tesque) supplemented with 5% fetal bovine serum (FBS). hTERT-RPE1 cells (CRL-4000; American Type Culture Collection) were grown in DMEM/Ham's F-12 medium (Nacalai Tesque) supplemented with 10% FBS and 0.348% sodium bicarbonate at 37°C in 5% CO_2. *IFT27*-KO cells (cell line #IFT27-2-2) and *CEP19*-KO cells (cell lines #CEP19-1-2 and #CEP19-1-12) were established from hTERT-RPE1 cells, as described previously (Nishijima *et al.*, 2017; Zhou *et al.*, 2022).

VIP assay and immunoblotting analysis

The VIP assay and subsequent immunoblotting analysis were carried out as described previously (Katoh *et al.*, 2015; Katoh *et al.*, 2018), with minor modifications (Nishijima *et al.*, 2017; Ishida *et al.*, 2021). Briefly, approximately 0.8×10^6 HEK293T cells were seeded onto 6-well plates, and on the next day, the cells were transfected with EGFP, mChe, and tBFP fusion constructs using Polyethylenimine Max and cultured for 24 h. The cells were then lysed in 250 µl of cell lysis buffer (20 mM HEPES-KOH [pH 7.4], 100 mM KCl, 5 mM NaCl, 3 mM $MgCl_2$, 1 mM dithiothreitol, 10% glycerol, and 0.1% Triton X-100) containing EDTA-free protease inhibitor cocktail (Nacalai Tesque). After 20 min on ice, the cell lysates were centrifuged at 16,100 × *g* for 15 min at 4°C in a microcentrifuge. The supernatants (200 µl) were incubated with 5 µl of GST-tagged anti-GFP Nb (Katoh *et al.*, 2015) or anti-mChe Nb (the LaM-2 version) (Ishida *et al.*, 2021) prebound to glutathione-Sepharose 4B beads for 1 h at 4°C. The beads were then washed three times with 180 µl of cell lysis buffer. The precipitated beads were transferred to a 96-well glass-bottomed plate (AGC Techno Glass) and observed using an all-in-one-type fluorescence microscope EVOS M5000 (Thermo Fisher Scientific) using a 10× /0.40 objective lens under constant conditions in the same set of experiments.

After microscopy, the beads were boiled in SDS–PAGE sample buffer, and the proteins were separated by SDS–PAGE and electroblotted onto an Immobilon-P PVDF membrane (Merck). The membrane was then blocked in 5% skimmed milk and incubated sequentially with a primary antibody (anti-GFP or anti-mChe) and peroxidase–conjugated secondary antibody. Protein bands were detected using a Chemi-Lumi One L kit (Nacalai Tesque), and images were captured using Amersham ImageQuant 800 (Cytiva).

Preparation of lentiviral vectors and establishment of stable cell lines

Lentiviral vectors for the stable expression of RABL2 constructs were prepared as previously described (Takahashi *et al.*, 2012; Hamada *et al.*, 2018). Briefly, HEK293T cells were cotransfected with an EGFP-fused RABL2 (WT) or RABL2 (Q80L) construct in pRRLsinPPT, and the packaging plasmids (pRSV-REV, pMD2.g, and pMDLg/pRRE [Thomas *et al.*, 2009]; kind gifts from Peter McPherson, McGill University) using Polyethylenimine Max. Culture medium was replaced 8 h after transfection and collected at 24, 36, and 48 h after transfection. The medium containing viral particles was passed through a 0.45-µm filter and centrifuged at 32,000 × *g* at 4°C for 4 h to precipitate the viral particles. The viral particles were resuspended in Opti-MEM (Thermo Fisher Scientific) and stored at −80°C until use. RPE1 cells and *CEP19*-KO cells that stably express an EGFP-RABL2 construct were prepared by addition of the lentiviral suspension to the culture medium.

Immunofluorescence analysis

The induction of ciliogenesis and subsequent immunofluorescence analysis of hTERT-RPE1 cells were performed as described previously (Nishijima *et al.*, 2017; Zhou *et al.*, 2022). Cells on coverslips were fixed with 3% paraformaldehyde for 10 min at 37°C and permeabilized with 0.1% Triton X-100 for 5 min at room temperature (for experiments shown in Figure 2, A–G), fixed with 3% paraformaldehyde for 5 min at 37°C, permeabilized with 100% methanol for 5 min at −20°C (for experiments shown in Figures 3, A–G, 4, A–N, and 5, A–N), fixed with 10% trichloroacetic acid for 15 min on ice, and permeabilized with 0.1% Triton X-100 for 5 min at room temperature (for experiments shown in Figure 3H–N) or fixed and permeabilized with 100% methanol for 5 min at −20°C (for Supplemental Figure S2). The fixed/permeabilized cells were washed three times with phosphate-buffered saline, blocked with 10% FBS, and incubated sequentially with primary and secondary antibodies diluted in Can Get Signal Immunostain Solution A (Toyobo) (for the detection of SMO) or in 5% FBS (for the detection of the other proteins). The cells were then observed using an Axio Observer microscope (Carl Zeiss). A region of interest (ROI) was created by drawing a line of 3-point width along the signal of ARL13B or Ac-tubulin within cilia using a segmented line tool in the ZEN 3.1 imaging software (Carl Zeiss). For the correction of local background intensity, the ROI was duplicated and set to a nearby region. Statistical analyses were performed using GraphPad Prism8 (version 8.4.3; GraphPad Software, Inc.).

ACKNOWLEDGMENTS

We thank Peter McPherson for providing the plasmids for production of recombinant lentiviruses and Helena Akiko Popiel for critical reading of the manuscript. This work was supported in part by grants from the Japan Society for the Promotion of Science (Grant Numbers 19H00980 and 20H04904 to K.N. and 21H02427 to Y.K.) and a grant of JRPs-LEAD with UKRI from the Japan Society for the Promotion of Science (Grant Number JPJSJRP20181701 to K.N.). Z. Z. received financial support from the Otsuka-Toshimi Scholarship Foundation.

REFERENCES

Anvarian Z, Mykytyn K, Mukhopadhyay S, Pedersen LB, Christensen ST (2019). Cellular signaling by primary cilia in development, organ function and disease. Nat Rev Nephrol 15, 199–219.

Badgandi HB, Hwang S, Shimada IS, Loriot E, Mukhopadhyay S (2017). Tubby family proteins are adaptors for ciliary trafficking of integral membrane proteins. J Cell Biol 216, 743–760.

Barbeito R, Tachibana Y, Martin-Morales R, Moreno P, Mykytyn K, Kobayashi T, Garcia-Gonzalo FR (2021). HTR6 and SSTR3 ciliary trageting relies on both IC3 loops and C-terminal tails. Life Sci Alliance 4, e202000746.

Bhogaraju S, Cajánek L, Fort C, Blisnick T, Weber K, Taschner M, Mizuno N, Lamla S, Bastin P, Nigg EA, Lorentzen E (2013). Molecular basis of tubulin transport within the cilium by IFT74 and IFT81. Science 341, 1009–1012.

Bhogaraju S, Taschner M, Morawetz M, Basquin C, Lorentzen E (2011). Crystal structure of the intraflagellar transport complex 25/27. EMBO J 30, 1907–1918.
Boldt K, van Reeuwijk J, Lu Q, Koutroumpas K, Nguyen TM, Texier Y, van Beersum SEC, Horn N, Willer JR, Mans D, *et al*. (2016). An organelle-specific protein landscape identifies novel diseases and molecular mechanisms. Nat Commun 7, 11491.
Bölükbaşi EY, Mumtaz S, Afzal M, Woehlbier U, Malik S, Tolun A (2018). Homozygous mutation in *CEP19*, a gene mutated in morbid obesity, in Bardet-Biedl syndrome with predominant postaxial polydactyly. J Med Genet 55, 189–197.
Braun DA, Hildebrandt F (2017). Ciliopathies. Cold Spring Harb Perspect Biol 9, a028191.
Bujakowska KM, Zhang Q, Siemiakowska AM, Liu Q, Place E, Falk MJ, Consugar M, Lancelot M-E, Antonio A, Lonjou C, *et al*. (2015). Mutations in *IFT172* causes isolated retinal degeneration and Bardet-Biedl syndorme. Hum Mol Genet 24, 230–242.
Cole DG, Diener DR, Himelblau AL, Beech PL, Fuster JC, Rosenbaum JL (1998). *Chlamydomonas* kinesin-II-dependent intraflagellar transport (IFT): IFT particles contain proteins required for ciliary assembly in Caenorhabditis elegans sensory neurons. J Cell Biol 144, 993–1008.
Dateyama I, Sugihara Y, Chiba S, Ota R, Nakagawa R, Kobayashi T, Itoh H (2019). RABL2 positively controls localization of GPCRs in mammalian primary cilia. J Cell Sci 132, jcs224428.
Desai PB, Stuck MW, Lv B, Pazour GJ (2020). Ubiquitin links smoothened to intraflagellar transport to regulate Hedgehog signaling. J Cell Biol 219, e201912104.
Dong B, Wu S, Wang J, Liu Y-X, Peng Z, Meng D-M, Huang K, Wu M, Fan Z-C (2017). *Chlamydomonas* IFT25 is dispensable for flagellar assembly but required to export the BBSome from flagella. Biol Open 6, 1680–1691.
Duan S, Li H, Zhang Y, Yang S, Chen Y, Qiu B, Huang C, Wang J, Li J, Zhu X, Yan X (2021). Rabl2 GTP hydrolysis licenses BBSome-mediated export to fine-tune ciliary signaling. EMBO J 40, e105499.
Eguether T, San Agustin JT, Keady BT, Jonassen JA, Liang Y, Francis R, Tobita K, Johnson CA, Abdelhamed ZA, Lo CW, Pazour GJ (2014). IFT27 links the BBSome to IFT for maintenance of the ciliary signaling compartment. Dev Cell 21, 279–290.
Funabashi T, Katoh Y, Okazaki M, Sugawa M, Nakayama K (2018). Interaction of heterotrimeric kinesin-II with IFT-B-connecting tetramer is crucial for ciliogenesis. J Cell Biol 217, 2867–2876.
Garcia-Gonzalo FR, Reiter JF (2017). Open sesame: how transition fibers and the transition zone control ciliary composition. Cold Spring Harb Perspect Biol 9, a028134.
Gonçalves J, Pelletier L (2017). The ciliary transition zone: finding the pieces and assembling the gate. Mol Cells 40, 243–253.
Hamada Y, Tsurumi Y, Nozaki S, Katoh Y, Nakayama K (2018). Interaction of WDR60 intermediate chain with TCTEX1D2 light chain of the dynein-2 complex is crucial for ciliary protein trafficking. Mol Biol Cell 29, 1628–1639.
Hirano M, Satake W, Moriyama N, Saida K, Okamoto N, Cha P-C, Suzuki Y, Kusunoki S, Toda T (2020). Bardet-Biedl syndrome and related disorders in Japan. J Hum Genet 65, 847–853.
Hirano T, Katoh Y, Nakayama K (2017). Intraflagellar transport-A complex mediates ciliary entry and retrograde trafficking of ciliary G protein-coupled receptors. Mol Biol Cell 28, 429–439.
Ishida Y, Kobayashi T, Chiba S, Katoh Y, Nakayama K (2021). Molecular basis of ciliary defects caused by compound heterozygous *IFT144/WDR19* mutations found in cranioectodermal dysplasia. Hum Mol Genet 30, 213–225.
Jiang J, Promchan K, Jiang H, Awasthi P, Marshall H, Harned A, Natarajan V (2016). Depletion of BBS protein LZTFL1 affects growth and causes retinal degeneration in mice. J Genet Genom 43, 381–391.
Jordan MA, Diener DR, Stepanek L, Pigino G (2018). The cryo-EM structure of intraflagellar transport trains reveals how dynein is inactivated to ensure unidirectional anterogarde movement in cilia. Nat Cell Biol 20, 1250–1255.
Kanie T, Abbott KL, Mooney NA, Plowey ED, Demeter J, Jackson PK (2017). The CEP19-RABL2 GTPase complex binds to IFT-B to initiate intraflagellar transport at the ciliary base. Dev Cell 42, 22–36.
Katoh Y, Chiba S, Nakayama K (2020). Practical method for superresolution imaging of primary cilia and centrioles by expansion microscopy using an amplibody for fluorescence signal amplification. Mol Biol Cell 31, 2195–2206.
Katoh Y, Nakamura K, Nakayama K (2018). Visible immunoprecipitation (VIP) assay: a simple and versatile method for visual detection of protein-protein interactions. Bio-protocol 8, e2687.
Katoh Y, Nozaki S, Hartanto D, Miyano R, Nakayama K (2015). Architectures of multisubunit complexes revealed by a visible immunoprecipitation assay using fluorescent fusion proteins. J Cell Sci 128, 2351–2362.
Katoh Y, Terada M, Nishijima Y, Takei R, Nozaki S, Hamada H, Nakayama K (2016). Overall architecture of the intraflagellar transport (IFT)-B complex containing Cluap1/IFT38 as an essential component of the IFT-B peripheral subcomplex. J Biol Chem 291, 10962–10975.
Keady BT, Samtani R, Tobita K, Tsuchiya M, San Augstin JT, Follit JA, Jonassen JA, Subramanian R, Lo CW, Pazour GJ (2012). IFT25 links the signal-dependent movement of hedgehog components to intraflagellar transport. Dev Cell 22, 940–951.
Kiesel P, Viar GA, Tsoy N, Maraspini R, Gorilak P, Varga V, Honigmann A, Pigino G (2020). The molecular structure of mammalian primary cilia revealed by cryo-electron tomography. Nat Struct Mol Biol 27, 1115–1124.
Kobayashi T, Ishida Y, Hirano T, Katoh Y, Nakayama K (2021). Cooperation of the IFT-A complex with the IFT-B complex is required for ciliary retrograde protein trafficking and GPCR import. Mol Biol Cell 32, 45–56.
Kopinke D, Norris AM, Mukhopadhyay S (2021). Developmental and regenerative paradigms of cilia regulated hedgehog signaling. Sem Cell Dev Biol 110, 89–103.
Kramer M, Backhaus O, Rosenstiel P, Horn D, Klopocki E, Birkenmeier G, Schreiber S, Platzer M, Hampe J, Huse K (2010). Analysis of relative gene dosage and expression differences of the paralogs RABL2A and RABL2B by pyrosequencing. Gene 455, 1–7.
Kubo T, Brown JM, Bellve K, Craige B, Craft JM, Fogarty K, Lechtreck K-F, Witman GB (2016). The IFT81 and IFT74 N-termini together form the major module for intraflagellar transport of tubulin. J Cell Sci 129, 2106–2119.
Lechtreck K-F, Brown JM, Sampaio JL, Craft JM, Shevchenko A, Evans JE, Witman GB (2013). Cycling of the signaling protein phospholipase D through cilia requires the BBSome only for the export phase. J Cell Biol 201, 249–261.
Liew GM, Ye F, Nager AR, Murphy JP, Lee JSH, Aguiar M, Breslow DK, Gygi SP, Nachury MV (2014). The intraflagellar transport protein IFT27 promotes BBSome exit from cilia through the GTPase ARL6/BBS3. Dev Cell 31, 265–278.
Liu P, Lechtreck KF (2018). The Bardet-Biedl syndrome protein complex is an adaptor expanding the cargo of range of intraflagellar transport trains for ciliary export. Proc Natl Acad Sci USA 115, E934–E943.
Liu Y-X, Xue B, Sun W-Y, Wingfield JL, Sun J, Wu M, Lechtreck KF, Wu Z, Fan Z-C (2021). Bardet-Biedl syndrome 3 protein promotes ciliary exit of the signaling protein phospholipase D via the BBSome. eLife 10, e59119.
Lo JCY, O'Connor AE, Andrews ZB, Lo C, Tiganis T, Watt MJ, O'Bryan MK (2016). RABL2 is required for hepatic fatty acid homeostasis and its dysfunction leads to steatosis and a diabetes-like state. Endocrinology 157, 4732–4743.
Lv B, Stuck MW, Desai PB, Cabrera OA, Pazour GJ (2021). E3 ubiqutin ligase Wwp1 regulates ciliary dynamics of the Hedgehog receptor Smoothened. J Cell Biol 220, e202010177.
Mencarelli C, Mitchell A, Leoncini R, Rosenbaum J, Lupetti P (2013). Isolation of intraflagellar transport trains. Cytoskeleton 70, 439–452.
Mick DU, Rodrigues RB, Leib RD, Adams CM, Chien AS, Gygi SP, Nachury MV (2015). Proteomics of primary cilia by proximity labeling. Dev Cell 35, 497–512.
Mukhopadhyay S, Wen X, Chih B, Nelson CD, Lane WS, Scales SJ, Jackson PK (2010). TULP3 bridges the IFT-A complex and membrane phosphoinositides to promote trafficking of G protein-coupled receptors into primary cilia. Genes Dev 24, 2180–2193.
Nachury MV, Mick DU (2019). Establishing and regulating the composition of cilia for signal transduction. Nat Rev Mol Cell Biol 20, 389–405.
Nakayama K, Katoh Y (2018). Ciliary protein trafficking mediated by IFT and BBSome complexes with the aid of kinesin-2 and dynein-2 motors. J Biochem 163, 155–164.
Nakayama K, Katoh Y (2020). Architecture of the IFT ciliary trafficking machinery and interplay between its components. Crit Rev Biochem Mol Biol 55, 179–196.
Nishijima Y, Hagiya Y, Kubo T, Takei R, Katoh Y, Nakayama K (2017). RABL2 interacts with the intraflagellar transport B complex and CEP19 and participates in ciliary assembly. Mol Biol Cell 28, 1652–1666.
Nozaki S, Castro Araya RF, Katoh Y, Nakayama K (2019). Requirement of IFT-B–BBSome complex interaction in export of GPR161 from cilia. Biol Open 8, bio043786.

Nozaki S, Katoh Y, Kobayashi T, Nakayama K (2018). BBS1 is involved in retrograde trafficking of ciliary GPCRs in the context of the BBSome complex. PLoS ONE 13, e0195005.
Park J, Lee J, Shim J, Han W, Lee J, Bae YC, Chung YD, Kim CH, Moon SJ (2013). dTULP, the *Drosophila melanogaster* homolog of Tubby, regulates transient receptor potential channel localization in cilia. PLoS Genet 9, e1003814.
Picariello T, Brown JM, Hou Y, Swank G, Cochran DA, King OD, Lechtreck K, Pazour GJ, Witman GB (2019). A global analysis of IFT-A function reveals specialization for transport of membrane-associated proteins into cilia. J Cell Sci 132, jcs220749.
Reiter JF, Leroux MR (2017). Genes and molecular pathways underpinning ciliopathies. Nat Rev Mol Cell Biol 18, 533–547.
Rosenbaum JL, Witman GB (2002). Intraflagellar transport. Nat Rev Mol Cell Biol 3, 813–825.
Satoda Y, Noguchi T, Fujii T, Taniguchi A, Katoh Y, Nakayama K (2022). BROMI/TBC1D32 together with CCRK/CDK20 and FAM149B1/JBTS36 contributes to IFT turnaround involving ICK/CILK1. Mol Biol Cell 33, ar79.
Schaefer E, Stoetzel C, Scheidecker S, Geoffroy V, Prasad MK, Redin C, Missotte I, Lacombe D, mandel J-L, Muller J, Dollfus H (2016). Identification of a novel mutation confirms the implication of *IFT172* (*BBS20*) in Bardet-Biedl syndrome. J Hum Genet 61, 447–450.
Seo S, Zhang Q, Bugge K, Breslow DK, Searby CC, Nachury MV, Sheffield VC (2011). A novel protein LZTFL1 regulates ciliary trafficking of the BBSome and Smoothened. PLoS Genet 7, e1002358.
Shalata A, Ramirez MC, Desnick RJ, Priedigkeit N, Buettner C, Lindtner C, Mahroum M, Abdul-Ghani M, Dong F, Arar N, *et al*. (2013). Morbid obesity resulting from inactivation of the ciliary protein CEP19 in humans and mice. Am J Hum Genet 93, 1061–1071.
Shinde SR, Nagar AR, Nachury MV (2020). Ubiquitin chains earmark GPCRs for BBSome-mediated removal from cilia. J Cell Biol 219, e202003020.
Sun W-Y, Xue B, Liu Y-X, Zhang R-K, Li R-C, Xin W, Wu M, Fan Z-C (2021). *Chlamydomonas* LZTFL1 mediates phototaxis via controlling BBSome recruitment to the basal body and its reassembly at the ciliary tip. Proc Natl Acad Sci USA 118, e101590118.
Takahashi S, Kubo K, Waguri S, Yabashi A, Shin H-W, Katoh Y, Nakayama K (2012). Rab11 regulates exocytosis of recycling vesicles at the plasma membrane. J Cell Sci 125, 4049–4057.
Taschner M, Bhogaraju S, Vetter M, Morawetz M, Lorentzen E (2011). Biochemical mapping of interactions within the intraflagellar transport (IFT) B core complex: IFT52 binds directly to four other IFT-B subunits. J Biol Chem 286, 26344–26352.
Taschner M, Kotsis F, Braeuer P, Kuehn EW, Lorentzen E (2014). Crystal structures of IFT70/52 and IFT52/46 provide insight into intraflagellar transport B core complex assembly. J Cell Biol 207, 269–282.
Taschner M, Lorentzen E (2016). The intraflagellar transport machinery. Cold Spring Harb Perspect Biol 8, a028092.
Taschner M, Weber K, Mourão A, Vetter M, Awasthi M, Stiegler M, Bhogaraju S, Lorentzen E (2016). Intraflagellar transport proteins 172, 80, 57, 54, 38, and 20 form a stable tubulin-binding IFT-B2 complex. EMBO J 35, 773–790.
Thomas S, Ritter B, Verbich D, Sanson C, Bourbonnière L, McKinney RA, McPherson PS (2009). Intersectin regulates dendritic spine development and somatodendritic endocytosis but not synaptic vesicle recycling in hippocampal neurons. J Biol Chem 284, 12410–12419.
Tsurumi Y, Hamada Y, Katoh Y, Nakayama K (2019). Interactions of the dynein-2 intermediate chain WDR34 with the light chains are required for ciliary retrograde protein trafficking. Mol Biol Cell 30, 658–670.
van den Hoek H, Klena N, Jordan MA, Viar GA, Righetto RD, Schaffer M, Erdmann PS, Wan W, Geimer S, Plitzko JM, *et al*. (2022). In situ architecture of the ciliary base reveals the stepwise assembly of intraflagellar transport trains. Science 377, 543–548.
Wachter S, Jung J, Shafiq S, Basquin J, Fort C, Bastin P, Lorentzen E (2019). Binding of IFT22 to the intraflagellar transport complex is essential for flagellum assembly. EMBO J 38, e101251.
Wang Z, Fan ZC, Williamson SM, Qin H (2009). Intraflagellar transport (IFT) protein IFT25 is a phosphoprotein component of IFT complex B and physically interacts with IFT27 in *Chlamydomonas*. PLoS One 4, e5384.
Wingfield JL, Mengoni I, Bomberger H, Jiang YY, Walsh JD, Brown JM, Picariello T, Cochran DA, Zhu B, Pan J, *et al*. (2017). IFT trains in different stages of assembly queue at the ciliary base for consecutive release into the cilium. eLife 6, e26609.
Yan X, Shen Y (2022). Rab-like small GTPases in the regulation of ciliary Bardet-Biedl syndrome (BBS) complex transport. FEBS J, https://doi.org/10.1111/febs.16232.
Yang S, Bahl K, Chou H-T, Woodsmith J, Stelzl U, Walz T, Nachury MV (2020). Near-atomic structures of the BBSome reveal the basis for BBSome activation and binding to GPCR cargoes. eLife 9, e55954.
Yang TT, Su J, Wang W-J, Craige B, Witman GB, Tsou M-FB, Liao J-C (2015). Superresolution pattern recognition reveals the architectural map of the ciliary transition zone. Sci Rep 5, 14096.
Yang TT, Tran MNT, Chong WM, Huang C-E, Liao J-C (2019). Single-particle tracking localization microscopy reveals nonaxonemal dynamics of intraflagellar transport proteins at the base of mammalian promary cilia. Mol Biol Cell 30, 828–837.
Ye F, Nager AR, Nachury MV (2018). BBSome trains remove activated GPCRs from cilia by enabling passage through the transition zone. J Cell Biol 217, 1847–1868.
Zhou Z, Qiu H, Castro-Araya R-F, Takei R, Nakayama K, Katoh Y (2022). Impaired cooperation between IFT74/BBS22–IFT81 and IFT25–IFT27/BBS19 in the IFT-B complex causes ciliary defects in Bardet-Biedl syndrome. Hum Mol Genet 31, 1681–1693.